Theoretical analysis of dielectric-loaded surface plasmon-polariton waveguides

Tobias Holmgaard* and Sergey I. Bozhevolnyi
Department of Physics and Nanotechnology, Aalborg University, Skjernvej 4A, DK-9220 Aalborg Øst, Denmark
(Received 15 December 2006; revised manuscript received 16 March 2007; published 6 June 2007)

Waveguiding of surface plasmon-polaritons (SPPs) by a dielectric ridge placed on a metal surface is analyzed using the effective-index method (EIM) and the finite element method (FEM). Main characteristics of these dielectric-loaded SPP waveguide (DLSPPW) structures, i.e., the mode effective index, confinement, and propagation length, are calculated at the telecom wavelength $\lambda = 1.55$ μm for different widths and thicknesses of a polymer ridge (with the refractive index of 1.535) placed on a gold film surface. The condition for single-mode guiding is investigated using the EIM, and it is found that single-mode DLSPPW guiding can be realized for ridge thicknesses smaller than ~630 nm and widths below ~655 nm (when decreasing the ridge thickness, the ridge width suitable for single-mode guiding increases). It is also established that, in contrast to the usual trade-off, the DLSPPW mode lateral confinement can be improved simultaneously with the increase in the mode propagation length by choosing the appropriate ridge thickness. The accuracy of the EIM is evaluated by comparing the computed mode characteristics with those obtained with the FEM and found rather good for the modes being far from cutoff.

DOI: 10.1103/PhysRevB.75.245405 PACS number(s): 73.20.Mf, 71.36.+c, 78.20.Bh, 42.79.Gn

I. INTRODUCTION

The recent explosive growth of research into plasmonics has been largely stimulated by the expectation that plasmonic circuits would be able of combining the best sides of electronic (with respect to physical dimensions) and optical (with respect to operation speed) circuits. Plasmonic circuits are perceived as consisting of photonic components utilizing, in one or another form, surface plasmon-polaritons (SPPs), which are quasi-two-dimensional electromagnetic excitations, propagating along a metal-dielectric interface and having the field components decaying exponentially into both neighboring media.[1] The latter feature results in the SPP characteristics being a mixture of those found for waves in dielectric and metal media. Typically, SPPs are tightly bound to the metal surface penetrating ~100 nm in the dielectric and ~10 nm in the metal, a feature that implies the possibility of using SPPs for subwavelength optical interconnects and photonic circuits.[2] The main issue in this context is to strongly confine the SPP field in the cross section perpendicular to the SPP propagation direction (smaller cross sections ensure smaller bend losses and higher densities of components) while keeping relatively low propagation losses.

It has been shown using numerical simulations that nanometer-sized metal rods can support extremely confined SPP modes propagating though only over hundreds of nanometers.[3] Similar properties were expected[4] and indeed found[5] for the electromagnetic excitations supported by chains of metal nanospheres. SPP propagation along metal stripes[6] and channels in periodically corrugated regions[7] has also exhibited propagation losses increasing drastically with the decrease in the stripe or channel width. Recently, SPP gap waveguides based on the SPP propagation between profiled metal surfaces have been suggested[8] and various nanowaveguide configurations have been modeled.[9] Quite recently, channel SPP modes, or channel plasmon-polaritons (CPPs),[10] where the electromagnetic radiation is concentrated at the bottom of V-shaped grooves milled in a metal film, have been first predicted[11] and then experimentally shown[12] to exhibit useful subwavelength confinement and moderate propagation loss. Moreover, various CPP-based subwavelength waveguide components, including Mach-Zehnder interferometers and waveguide-ring resonators, have been successfully realized.[13] It should be noted though that, in general, the SPP confinement is achieved primarily by decreasing the SPP spatial extent into the dielectric, thereby increasing the portion of SPP power being absorbed by the metal, so that the choice of optimum guiding configuration is subject to trade-off with many intricate issues yet to be elucidated.

In conventional integrated optics, one can drastically reduce a waveguide mode size in the lateral cross section by employing high-index-contrast waveguides, i.e., waveguides having a core refractive index significantly different from that in surrounding media.[14] A similar approach involving SPP modes has also been very recently demonstrated.[15,16] The configuration used consists of a dielectric ridge placed on a metal surface, and the lateral SPP confinement is achieved due to the fact that the SPP effective index is larger for the SPP mode supported by the metal-dielectric interface (even for thin dielectric layers) than for that supported by the air-metal interface.[17] Borrowing an analogous term from integrated optics,[18,19] such a waveguide configuration will be hereafter called the dielectric-loaded SPP waveguide (DLSPPW) configuration. The reported experimental results have already indicated that the DLSPPWs can indeed be used for efficient guiding of SPP modes.[15,16] Some of the DLSPPW characteristics have also been modeled with the effective-index approximation,[15] but there are a number of very important issues, e.g., the aforementioned trade-off, that require detailed and careful theoretical consideration using accurate modeling tools.

The effective-index method (EIM) is one of the standard methods for analysis of photonic and SPP waveguides, which is known to yield reasonably accurate results for weakly guided (linearly polarized) modes being far from cutoff.[18–20] It has also been found useful when considering channel SPP

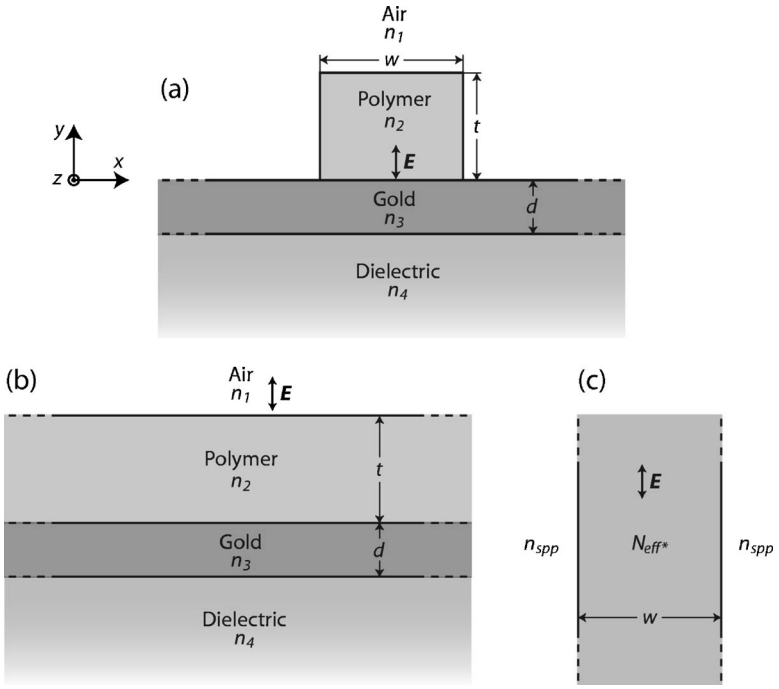

FIG. 1. (a) Cross-sectional view of the DLSPPW structure under investigation. (b) The four-layer and (c) three-layer structures considered correspondingly in the first and second steps of the EIM-1. The coordinate system used is also shown along with the orientation of the main component of the electric field in the case of TM modes.

modes.[21] Combined with the simplicity of the EIM, this makes it attractive for consideration of DLSPPW mode characteristics provided that its accuracy and validity domain are established. Various numerical methods such as the finite difference method,[22] the method of lines,[23] the finite difference time-domain algorithm,[11] and the finite element method[24] have previously been successfully utilized in the analysis of optical waveguides. In this paper, the DLSPPW mode effective index, confinement, and propagation lengths are investigated in detail using the EIM, and the results are compared to and complemented with those obtained by making use of the finite element method (FEM).

This paper is organized as follows. In Sec. II, the EIM is presented and used in calculations of the DLSPPW mode effective index, propagation length, and confinement for different system parameters. After this, the FEM is introduced and employed in Sec. III for calculations of field distributions and vector plots in the DLSPPW cross section. The accuracy of the EIM is evaluated in Sec. IV by comparing the mode effective index, propagation length, and vertical and lateral field profiles calculated with the EIM and FEM. Finally, in Sec. V, we discuss the results obtained and offer our conclusions.

II. EFFECTIVE-INDEX CALCULATION

The analyzed straight waveguide structure is similar to that investigated experimentally[16] and represents a dielectric (e.g., polymer) ridge with refractive index n_2, thickness t, and width w placed on a metal (e.g., gold) film with thickness d and wavelength dependent refractive index n_3 [Fig. 1(a)]. The gold-polymer structure is enclosed by air with refractive index n_1 above and a semi-infinite dielectric layer with refractive index n_4 below, which represents a thick glass substrate usually used in experiments to support the gold film with polymer ridge structures.[16]

In the EIM, the two-dimensional (2D) cross section of the DLSPPW is considered and solved for guided modes by dealing consecutively with two one-dimensional (1D) waveguide geometries, which can be solved individually in a manner similar to that used for analyzing multilayer waveguide structures.[25–27] The key assumption made in the reduction of the problem is that the modes are linearly polarized and well above cutoff, i.e., with most of the power concentrated in the ridge subregion so that the field magnitudes in the four corner regions are small enough to be neglected. Whereas the EIM previously has been used to analyze dielectric ridge waveguides,[25–27] which does not differ geometrically from DLSPPWs, the very large and complex refractive index of the gold film at telecom wavelengths potentially changes the validity of the EIM. The conclusions made on the performance of the EIM in contemplation of dielectric ridge waveguides can thus not be directly adapted to EIM calculations of DLSPPW modes.

One can view the 2D waveguide structure [Fig. 1(a)] as being obtained by decreasing the width of the top polymer layer [Fig. 1(b)] to match that of the ridge. The first step in such an EIM approach (here denoted EIM-1 to distinguish it from another EIM approach introduced later) is thus to calculate the effective index N_{eff}^{*} of guided modes in a planar four-layer waveguide structure [Fig. 1(b)]. Each of the four layers is considered of infinite lateral extension in the x direction. Furthermore, the top (air) and bottom (dielectric) layers abutting the polymer and gold films are considered semi-infinite in the (depth) y direction, which implies that there are no reflections from external boundaries, only from the gold and polymer interfaces.

In the second step of the EIM-1 (when shrinking the polymer layer in width), N_{eff}^{*} is used in the calculation of the final mode effective index N_{eff} by contemplation of a three-layer waveguide structure with vertical interfaces [Fig. 1(c)]. As the modes of interest in this work are bound to the gold-

polymer interface, the effective index of a SPP propagating along the gold-air interface (n_{SPP}) is used outside the ridge subregion.

In the simulation results presented hereafter, an excitation wavelength $\lambda=1.55$ μm, a gold layer thickness $d=100$ nm, and refractive indexes $n_1=1$, $n_2=1.535$, $n_3=0.55+i11.5$,[28] and $n_4=1.6$ are used when calculating DLSPPW mode characteristics unless noted otherwise.

A. SPP guiding in the four-layer structure

The direction of SPP propagation is considered along the z axis (Fig. 1) and the electric field can then be written in the form

$$\mathbf{E}=\mathbf{E}_p(y)\exp[i(\omega t-\beta z)], \tag{1}$$

where $\mathbf{E}_p$ denotes the components of the electric field, e.g., being in the case of TM modes in the (y,z) plane. β is the complex propagation constant $\beta=\beta'-i\beta''$ which is related to the mode effective index according to $\beta'=k_0N_{eff}^*=(2\pi/\lambda)N_{eff}^*$ and propagation length as $L^*=1/(2\beta'')$. It is instructive to consider the SPP dispersion relation of a metal-dielectric interface, which can be thought of as a limiting case of the considered configuration with the polymer film thickness t being either very small or very large. The corresponding SPP dispersion relation is given by[1]

$$\beta=k_0\sqrt{\frac{\epsilon_m\epsilon_d}{\epsilon_m+\epsilon_d}}, \tag{2}$$

with ϵ_m being the complex permittivity of the metal and ϵ_d being the permittivity of the dielectric.

When solving the four-layer planar geometry [Fig. 1(b)] for the effective index N_{eff}^* and propagation length L^* for various polymer film thicknesses, it is expected that, for very thin film layers, the fundamental mode becomes progressively close to a SPP propagating along the gold-air interface, i.e., $N_{eff}^*\rightarrow 1.0038$ and $L^*\rightarrow 339$ μm. Correspondingly, for very thick film layers, the results should approach those of a SPP at the gold-polymer interface, i.e., $N_{eff}^*\rightarrow 1.55$ and $L^*\rightarrow 92$ μm. In between these extremes, it is expected that the SPP mode effective index of the four-layer structure is monotonously decreasing with the film thickness, since an increasing part of the SPP field penetrates in the air above the polymer. Decreasing the film thickness, however, also has the effect of squeezing the field inside the polymer region, because optical fields tend to be confined in regions with higher refractive indexes. This implies that the field magnitude at the gold-polymer interface (and inside the gold) increases, resulting in greater absorption loss. One should therefore expect that the propagation length decreases with the film thickness until some point, where the field cannot be squeezed more into the polymer, reaching a minimum. Decreasing the film thickness further would result in a rapid increase in the field outside the polymer, and the propagation length would approach that of the SPP at the gold-air interface.

The results of the calculations performed by utilizing a multilayer waveguide program for solution of the four-layer structure confirm the expected behavior (Fig. 2). It should be mentioned that the accuracy of the multilayer waveguide program used was found to be very good by comparison with FEM calculations (with deviations being less than 0.1%) conducted for the same structure. In addition to the fundamental transverse magnetic (TM_0) mode, the second fundamental (TM_1) and the fundamental transverse electric (TE_0) modes are found. In the notation used, a TM mode refers to a SPP mode with dominating x component of the magnetic field and TE refers to transverse electric mode with dominating x component of the electric field. The fundamental TE_0 mode is included in order to evaluate the single-mode condition for DLSPPWs; however, it is not further analyzed as the second step in the EIM assumes SPP modes due to the use of n_{SPP}, thus making evaluation of TE modes erroneous. The cutoff thickness of the TM_1 mode is $t\sim 631$ nm and the TE_0 mode has cutoff at $t\sim 313$ nm, implying that below these thicknesses the corresponding modes do not exist. By controlling the polarization and limiting the film thickness (by 630 nm in our case), the single-mode guiding in such a four-layered structure is thereby achievable. Single-mode

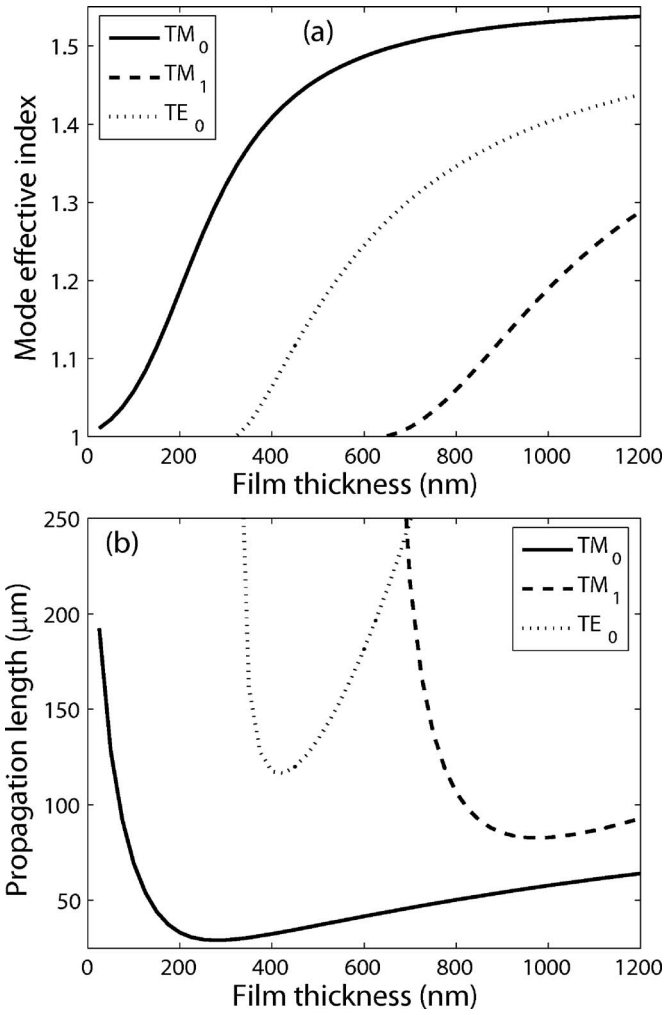

FIG. 2. Characteristics of modes supported by the four-layer structure presented in Fig. 1(b) and analyzed in the first step of the EIM-1. (a) The mode effective index and (b) the propagation length as a function of the film thickness for TM_0, TM_1, and TE_0 modes.

guiding allows one to avoid various mode dispersion and interference effects (usually unwanted) and is therefore preferential in photonic circuits. Conditions for the single-mode guiding in DLSPPWs are further considered in the following section.

B. Single-mode condition

The mode effective index of the DLSPPW [Fig. 1(a)] is found by utilizing the calculated effective index and propagation length of a multilayered structure (N_{eff}^{*} and L^{*}) and by taking into account the finite width of the ridge [Fig. 1(c)]. Although one can avoid the support of multiple modes of the multilayered structure [Fig. 1(b)] by limiting the ridge thickness to $t \lesssim 631$, care must be taken in the second step of the EIM-1 to avoid multimode guiding of the final structure. This is due to the possible appearance of TM_{01} modes, i.e., modes that have two peaks in the lateral profile. A condition for single-mode guiding of the DLSPPW is found by solving for the cutoff width of the TM_{01} mode, i.e., the minimum ridge width w which supports two TM modes. By designing ridges with widths below this cutoff width, single-mode guiding of the final waveguide structure is achievable. It is, however, apparent that the single-mode guiding still requires TM-polarized excitation in order to avoid excitation of TE modes.

It is seen that the waveguide structure is symmetric in the lateral direction [Fig. 1(c)]. The cutoff width for the TM_{01} mode can then be calculated by utilizing normalized waveguide parameters as follows:[29]

$$w = \frac{\pi}{k_0 \sqrt{(N_{eff}^{*})^2 - (n_{SPP})^2}}, \tag{3}$$

where n_{SPP} is the mode effective index of the SPP supported by the gold-air interface. The cutoff ridge width for the TM_{01} mode is thus dependent on the wavelength and ridge thickness t as N_{eff}^{*} depends on the thickness t. For small thicknesses, N_{eff}^{*} approaches n_{SPP} and the cutoff ridge width increases rapidly. For large thicknesses, N_{eff}^{*} approaches the mode effective index of the SPP at the gold-polymer interface, and the cutoff ridge width approaches a constant value of $w \sim 655$ nm.

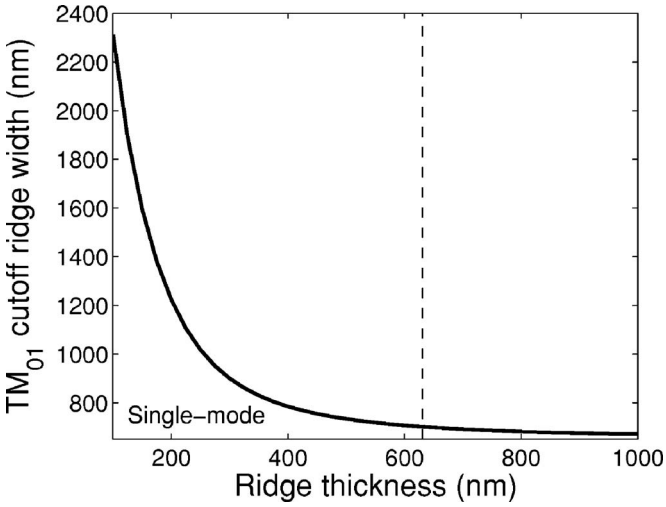

FIG. 3. Cutoff ridge width of the TM_{01} mode as a function of thickness. The vertical dashed line indicates the thickness where the TM_1 mode has cutoff.

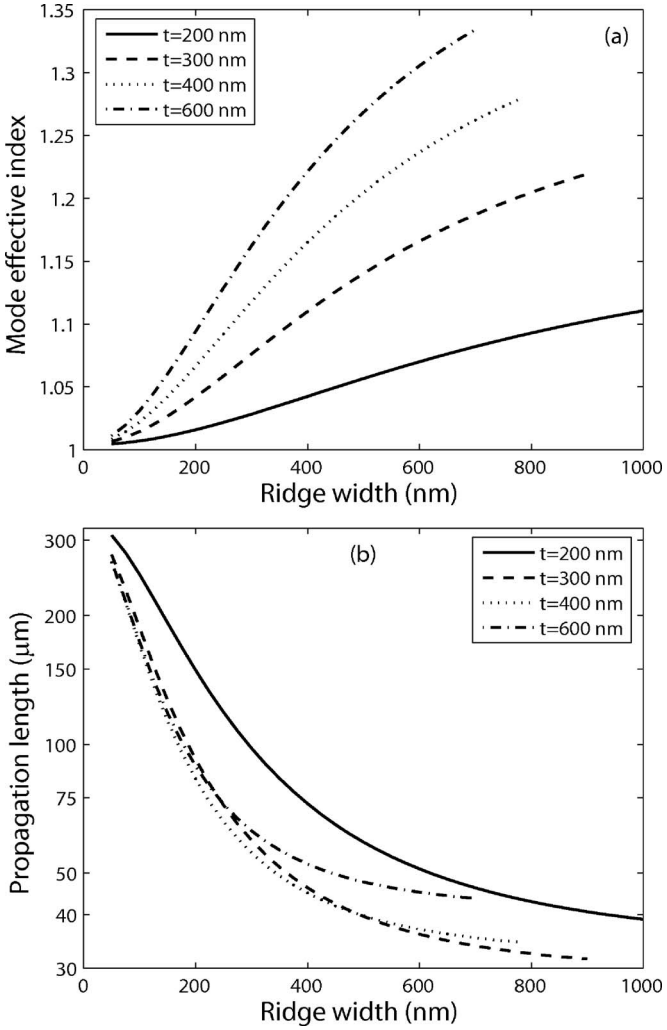

FIG. 4. The mode effective index and propagation length (logarithmic scale) as a function of ridge width for several different thicknesses as calculated with EIM-1. Each curve is ended at the cutoff width of the TM_{01} mode, i.e., where single-mode guiding ceases.

The cutoff ridge width of the TM_{01} mode was determined using Eq. (3) for different thicknesses by utilizing the calculated effective indexes N_{eff}^{*} (Fig. 3). It is apparent that the single-mode guiding in DLSPPWs is achieved in the parameter space below the (TM_{01}) cutoff width curve and to the left of the (TM_1) cutoff thickness line.

C. Fundamental mode characteristics

The mode effective indexes and propagation lengths of TM_{00} modes are found by solution of the three-layer structure [Fig. 1(c)] for different ridge dimensions (Fig. 4). For infinite ridge width, the structure and thus also the modes are identical to those of the four-layer structure [Fig. 1(b)], im-

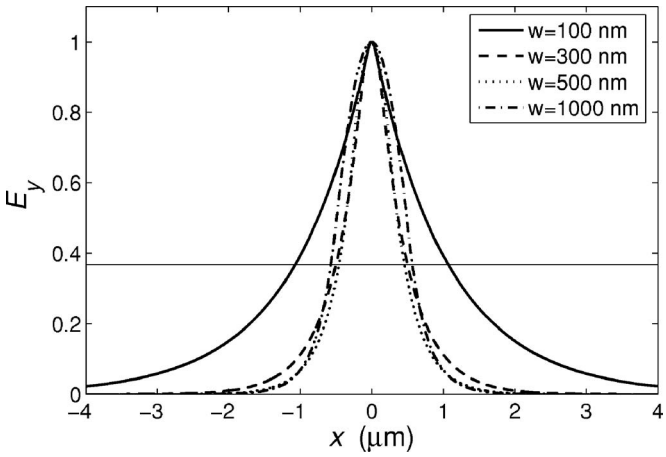

FIG. 5. The lateral field distribution of the main electric-field component for four widths w, all with $t=600$ nm. The thin horizontal line indicates the value $1/e$, and as the field profiles are scaled to a maximum value of 1, the mode width can be read from the intersection with this line. The calculations are performed with the EIM-1. The $w=1000$ nm waveguide is not single mode, but is included to illustrate that the mode width increases for wide ridges.

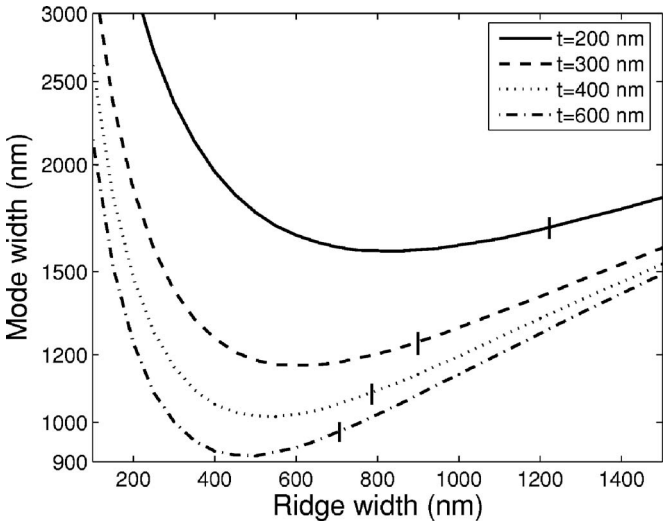

FIG. 6. The mode width (logarithmic scale) depicted versus the ridge width for four different values of ridge thickness t. The vertical lines crossing the curves mark the end of the single-mode regime. The calculations are performed by using the EIM-1.

plying that $N_{eff}\rightarrow N_{eff}^{*}$. As N_{eff}^{*} is increasing monotonously with thickness [Fig. 2(a)] so is N_{eff} [Fig. 4(a)]. A decrease in the ridge width decreases the field portion confined in the ridge region and the mode effective index therefore decreases. For very small ridge widths, the DLSPPW fundamental mode effective index N_{eff} approaches that of the SPP at the gold-air interface. Similar reasoning accounts for the propagation length of the mode, which increases when decreasing the ridge width and approaches the SPP propagation length at the gold-air interface [Fig. 4(b)]. The calculated propagation length dependence shows that a larger mode effective index (associated with a better mode confinement within the ridge) implies a shorter propagation length, in accordance with the general consideration. This, however, is strictly true only for constant-thickness ridge waveguides. For example, when comparing the length dependence for ridges with $t=600$ nm and $t=300$ nm, it is seen that the propagation length (of the DLSPPW fundamental mode) for the 600-nm-thick ridge waveguides is longer than that for 300-nm-thick ones once their widths are larger than 300 nm [Fig. 4(b)]. At the same time, the mode effective index for the 600-nm-thick ridge waveguides is larger than that for 300-nm-thick ones for all widths [Fig. 4(a)]. This feature is a consequence of the nonmonotone dependence of TM_0 propagation length [Fig. 2(b)], indicating also the possibility for optimization with respect to the confinement-loss trade-off.

D. Lateral mode field confinement

In the design of optical waveguides, the lateral mode field confinement is of great importance because a good confinement, i.e., a small mode width W, enables large bend angles $\theta\propto\lambda/W$ with acceptable bend losses, thereby minimizing the length of components $\ell\propto W/\theta$.[21] This trend in turn maximizes density of components $n\propto 1/(\ell W)=\lambda/W^3$ and, in addition, decreases the incurred propagation loss per component due to a decrease in the component length.

Previous results from contemplation of similar DLSPPW structures[15] illustrate that a large ridge curvature gives rise to a complete radiative loss of poorly confined SPP modes. This exemplifies the importance of well confined modes, and to accommodate this design parameter, the mode width of DLSPPWs of different dimensions is investigated in the following.

In order to find the mode width of the fundamental TM_{00} mode for different ridge dimensions, the field profiles of a lateral cross section are considered. The main electric-field component (E_y) of a lateral profile is considered for a 600-nm-thick ridge waveguide at four different widths (Fig. 5). Each profile has been normalized to a maximum value of 1 and the mode width is thus given as the width of the peak at a field value of $1/e$, represented by the thin horizontal line in the figure. The mode width is different for the four different thicknesses. It is very large for the 100-nm-wide ridge and seems to have a minimum around a ridge width of ~500 nm. This clearly illustrates that the field is squeezed into the ridge region when the width is decreased until a certain point, where the field no longer can be confined to the

TABLE I. The optimum ridge width regarding lateral field confinement along with the mode width, propagation length, and mode effective index for four different ridge thicknesses.

	t (nm)			
	200	300	400	600
w_{opt} (nm)	850	600	550	500
Mode width (nm)	1580	1165	1015	915
L (μm)	42	36	38	48
N_{eff}	1.10	1.17	1.22	1.27

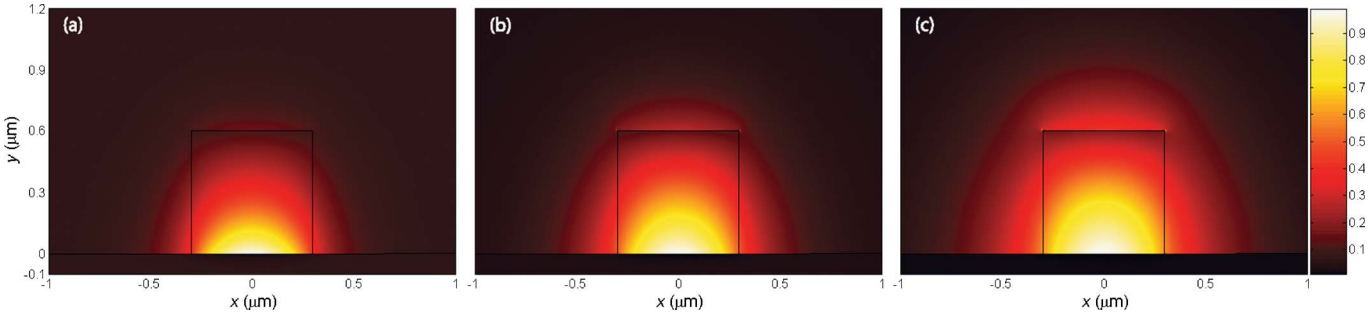

FIG. 7. (Color online) Field distribution plots of the magnitude of the vertical component of the electric field $|E_y|$ for ridge dimension $t=600$ nm, $w=600$ nm, calculated by application of the FEM. In all three plots, the fundamental TM_{00} mode is depicted. (a) shows the field for $\lambda=893$ nm $(n_3=0.21+i5.94)$ where $N_{eff}=1.49$ and $L=16.1$ μm, (b) for $\lambda=1.22$ μm $(n_3=0.36+i8.60)$ where $N_{eff}=1.39$ and $L=29.8$ μm, and (c) for $\lambda=1.55$ μm $(n_3=0.55+i11.5)$ where $N_{eff}=1.29$ and $L=44.4$ μm (Ref. 28).

ridge. Then, it starts to spread out into the surrounding air where the decay length is larger, thereby decreasing the mode confinement. To find the optimum width, regarding the mode width, for different ridge thicknesses, additional calculations have been performed (Fig. 6). The results show the mode width versus the ridge width for several different thicknesses. There is a distinct minimum in all curves, indicating the optimum ridge width w_{opt} regarding the lateral mode field confinement. The results for the five shown thicknesses are summarized in Table I, where w_{opt} along with the mode widths are shown for each of the five t values. The results presented here (Fig. 6 and Table I) show that in order to achieve good lateral mode field confinement, one should construct a DLSPPW of large thickness and width of 400–500 nm, e.g., $t=600$ nm and $w=500$ nm. Larger thicknesses are desirable regarding mode confinement and propagation length; however, since such waveguides are not single mode, they are not considered in this work.

III. FINITE ELEMENT CALCULATIONS

When utilizing the FEM to analyze the DLSPPW structure [Fig. 1(a)], the mode effective index, propagation length, and the magnetic- and electric-field vectors in the cross section of the DLSPPW can be found. In addition to providing numerically determined N_{eff} and L values, this method thus enables evaluation of some of the approximations made in the EIM-1, e.g., regarding strictly vertical polarization in the cross section of the waveguide.

The FEM is a technique for numerical solution of partial differential equations or integral equations. In the method, the region of interest is subdivided into small segments, usually triangles, and the partial differential equation is replaced with a corresponding functional. Subsequently, a variational method is used to minimize the functional in order to obtain variational features in the algorithm.[30–32]

The approach taken in the application of the FEM in this work is solution of the electric-field components and the propagation constant β. By assuming fields on a time-harmonic form, the wave equation for the electric field is given as

$$\nabla \times \left(\frac{1}{\mu_r} \nabla \times \mathbf{E} \right) - k_0^2 \epsilon_r \mathbf{E} = \mathbf{0}, \tag{4}$$

where the relative permittivity ϵ_r in general is a complex position dependent tensor and the relative permeability μ_r in general is a position dependent tensor. The media contemplated in this paper are, however, considered homogeneous, nonmagnetic, and isotropic, implying that ϵ_r has a constant scalar value within each medium and that $\mu_r=1$. With SPP propagation in the z direction, i.e.,

$$\mathbf{E}(x,y,z,t) = \mathbf{E}(x,y)\exp[i(\omega t - \beta z)], \tag{5}$$

the wave equation [Eq. (4)] simplifies to

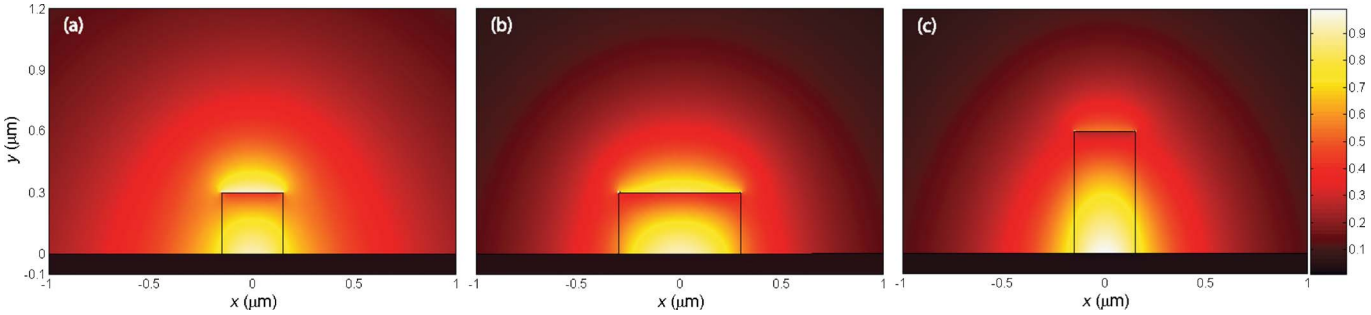

FIG. 8. (Color online) Field distribution plots of the magnitude of the vertical component of the electric field $|E_y|$ for different ridge dimensions. (a) shows $|E_y|$ for a $t=300$ nm, $w=300$ nm ridge where $N_{eff}=1.04$ and $L=68.7$ μm, (b) a $t=300$ nm, $w=600$ nm ridge where $N_{eff}=1.14$ and $L=37.0$ μm, and (c) a $t=600$ nm, $w=300$ nm ridge where $N_{eff}=1.13$ and $L=59.1$ μm.

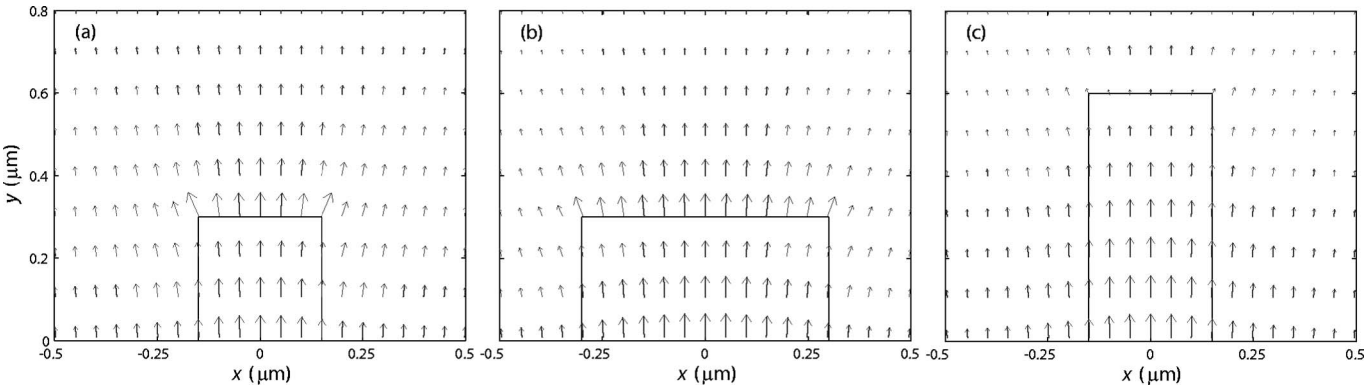

FIG. 9. Field vector plots of the electric field for different ridge dimensions. (a) shows $\mathbf{E}_t$ for a $t=300$ nm, $w=300$ nm ridge, (b) a $t=300$ nm, $w=600$ nm ridge, and (c) a $t=600$ nm, $w=300$ nm ridge. The field vectors are scaled arbitrarily.

$$\nabla_t^2 \mathbf{E} + (\epsilon_r k_0^2 - \beta^2)\mathbf{E} = \mathbf{0}, \tag{6}$$

where ∇_t^2 denotes the part of the Laplacian related to the transverse components (x,y). This is the partial differential equation from which a corresponding functional is constructed and solved for β, E_x, E_y, and E_z.

The boundary condition used at the exterior boundary (edge of computational window) is that of a perfect electric conductor,

$$\hat{\mathbf{n}} \times \mathbf{E} = \mathbf{0}, \tag{7}$$

which implies that the tangential components of the electric field are set to zero at the exterior boundary. The boundary conditions which must be fulfilled at the interior boundaries, i.e., at the interfaces between two media, are the continuity of the tangential components of the electric and magnetic fields and the continuity of the normal components of the electric and magnetic flux densities,

$$\hat{\mathbf{n}} \times (\mathbf{E}_1 - \mathbf{E}_2) = \mathbf{0}, \tag{8}$$

$$\hat{\mathbf{n}} \times (\mathbf{H}_1 - \mathbf{H}_2) = \mathbf{0}, \tag{9}$$

$$\hat{\mathbf{n}} \cdot (\mathbf{D}_1 - \mathbf{D}_2) = 0, \tag{10}$$

$$\hat{\mathbf{n}} \cdot (\mathbf{B}_1 - \mathbf{B}_2) = 0, \tag{11}$$

where it has been assumed that the surface charge density ρ_s and surface current density $\mathbf{J}_s$ are zero.

In the following two sections, field contour plots and field vector plots calculated by application of the FEM are treated, and in Sec. IV the calculated mode effective indexes and propagation lengths are compared to those found by means of the EIM. All FEM calculations in this work are performed by utilizing COMSOL MULTIPHYSICS 3.3.

A. Mode field cross-section distributions

The dependence of the field distribution of the y component of the electric field, the mode effective index, and the propagation length on SPP excitation wavelength and ridge dimensions is investigated. The field distribution of the fundamental TM_{00} mode of a DLSPPW is calculated for three different excitation wavelengths (Fig. 7). The dimension of the considered DLSPPW is $t=600$ nm, $w=600$ nm, and the results are shown for free-space excitation wavelengths of 893 nm, 1.22 μm, and 1.55 μm. As expected from the previous discussion, the field is strongly confined to the gold-polymer interface inside the ridge, indicating that the mode indeed is a DLSPPW mode, which is furthermore confirmed by the exponential decay into both the gold and polymer ridge regions (shown explicitly in the vertical field profiles presented in Sec. IV). The reasons for the nonevident field in the gold film in the field distribution plots are the conservation of the normal component of the electric flux density along with a large change in dielectric constant at the gold-polymer interface and the short penetration depth in the gold film. It is apparent that a shorter wavelength implies better confinement, as the ridge is optically larger for shorter wavelengths. Furthermore, a larger wavelength results in less loss and thus longer propagation lengths, in accordance with the

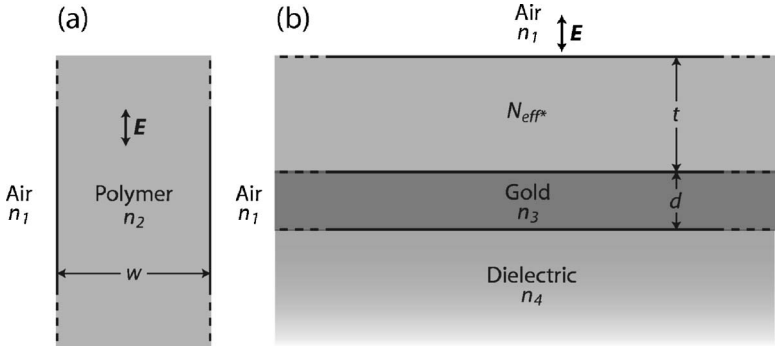

FIG. 10. Cross-sectional view of the waveguide structure considered (a) in the first step of the EIM-2 and (b) in the second step of the EIM-2. In both cases, the polarization is strictly vertical, and the layers are considered of infinite vertical and horizontal extents, respectively.

TABLE II. The mode effective indexes N_{eff} and propagation lengths L of the DLSPPWs calculated by means of the FEM, the EIM-1, and the EIM-2. The ridge thickness is constant at $t=600$ nm and the width varies from $w=200$ nm to $w=800$ nm.

	Ridge width (nm)						
	200	300	400	500	600	700	800
Mode index FEM	1.064	1.133	1.198	1.250	1.291	1.323	1.348
Mode index EIM-1	1.094	1.162	1.221	1.268	1.305	1.334	1.357
Mode index EIM-2	1.075	1.143	1.205	1.255	1.294	1.325	1.349
Prop. length (μm) FEM	81.3	59.1	50.1	46.4	44.4	42.8	42.2
Prop. length (μm) EIM-1	89.2	63.0	52.6	47.8	45.2	43.8	42.9
Prop. length (μm) EIM-2	104	78.6	66.3	59.4	55.1	52.2	50.2

general understanding. Due to the conservation of the normal component of the electric flux density at the interfaces [Eq. (10)], a discontinuous change in the electric field is expected at the lateral boundaries of the ridge. This discontinuity is very evident for the gold-polymer interface, but can also be observed for the air-polymer interface, however, less pronounced due to the smaller difference in permittivity.

The dependence of the field distribution of the vertical component of the electric field on ridge dimensions is calculated for an excitation wavelength of 1.55 μm (Fig. 8). Four different waveguide structures are considered in total [three in Fig. 8 and one in Fig. 7(c)]. The field distributions in a $t=300$ nm, $w=300$ nm ridge [Fig. 8(a)] and a $t=300$ nm, $w=600$ nm ridge [Fig. 8(b)] show that for small ridge thicknesses a large part of the field is distributed on top of the ridge waveguide, which is undesirable when designing optical components such as bends and splitters due to large radiative losses. Both $t=300$ nm waveguide structures also show a poor lateral confinement of the electric field in comparison with the $t=600$ nm ridge waveguides, which is in accordance with the EIM-1 results. The ridge dimensions which show the best confinement both laterally and vertically are clearly the largest ($t=600$ nm, $w=600$ nm [Fig. 7(c)]).

In the EIM, the field in the corner regions is disregarded, and for large ridges this appears to be a good approximation. Here, the field is mainly confined to the ridge and, in particular, to the gold-polymer interface. For small ridge dimensions, however, this approximation leads to an error, as a relatively large part of the field is concentrated in the two upper corner regions. The effect this has on the calculated mode effective indexes and propagation lengths is investigated in Sec. IV.

B. Electric-field orientation

In order to investigate the validity of the approximation made in the EIM of strictly vertical polarization, the field vectors of the electric field in the cross section of the DLSPPW, $\mathbf{E}_t$, are calculated for three different ridge dimensions by utilizing the FEM (Fig. 9). The field vectors of the small ridge ($t=300$ nm, $w=300$ nm [Fig. 9(a)]) show a quite large deviation from strictly vertical polarization. This is especially pronounced around the corners in the air surrounding the ridge, but it is evident in the entire plot except right through the middle of the ridge due to the symmetry of the ridge structure. The plot of the field vectors in the $t=300$ nm, $w=600$ nm structure [Fig. 9(b)] also shows nonvertical electric-field vectors, but since a larger part of the field is confined to the ridge, the deviation from vertical polarization is smaller. The $t=600$ nm, $w=300$ nm ridge structure [Fig. 9(c)] also shows less nonvertical polarization than

TABLE III. The mode effective indexes and propagation lengths of the DLSPPWs calculated by means of the FEM, the EIM-1, and the EIM-2. The ridge width is constant at $w=500$ nm and the thickness is varied.

	Ridge thickness (nm)						
	200	300	400	500	600	700	800
Mode index FEM	1.041	1.111	1.176	1.221	1.250	1.269	1.282
Mode index EIM-1	1.057	1.140	1.205	1.244	1.268	1.284	1.294
Mode index EIM-2	1.089	1.149	1.198	1.232	1.255	1.270	1.282
Prop. length (μm) FEM	66.0	41.7	39.5	42.2	46.4	50.4	54.8
Prop. length (μm) EIM-1	59.1	39.8	39.9	43.5	47.8	52.2	56.4
Prop. length (μm) EIM-2	61.9	51.3	51.2	54.6	59.4	64.5	69.6

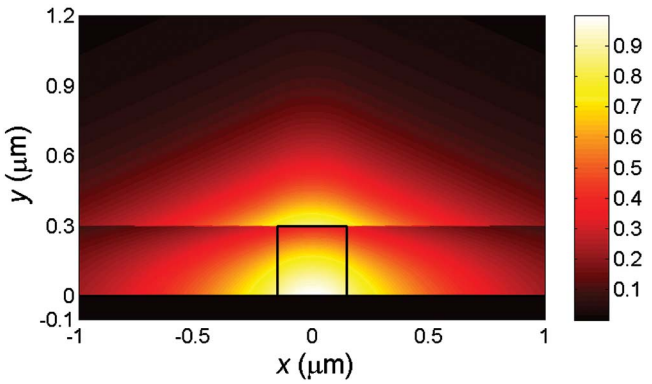

FIG. 11. (Color online) Field distribution of the magnitude of the vertical component of the electric field obtained by combining lateral and vertical field profiles from the EIM-1 for a $t=300$ nm, $w=300$ nm ridge.

the smaller structure, but there is still deviation evident in the corner regions outside the ridge. The variance from vertical polarization will cause discrepancy in the calculated mode effective indexes and propagation lengths of the two methods. The effect of this is investigated further in the following, where the accuracy of another EIM is also evaluated.

IV. COMPARISON OF SIMULATION METHODS

In order to investigate the validity of the EIM-1 results, the calculated mode effective indexes and propagation lengths are compared to those calculated by means of the FEM. Furthermore, the results of another effective-index approach (EIM-2) are compared to the FEM and EIM-1 results. The 2D waveguide geometry considered in the EIM-2 is the same as that of the EIM-1 [Fig. 1(a)]; however, a different approach is taken in the reduction of the 2D geometry to two 1D waveguide structures that can be dealt with consecutively (Fig. 10). First, an infinitely tall ridge is considered, i.e., an air-polymer-air layer with infinitely extending vertical boundaries [Fig. 10(a)]. A ridge width dependent effective index N_{eff}^{*} of this structure is calculated by assuming polarization parallel to the interfaces. One can then view the appearance of a DLSPPW by truncating the air-polymer-air structure vertically and surrounding it by air above and a gold-dielectric structure below. The effective index N_{eff}^{*} found by solution of the three-layer vertical structure is thus used in the solution of a four-layer planar waveguide structure, where infinite horizontal extension of the layers is assumed [Fig. 10(b)].

A. Mode effective index and propagation loss

The mode effective indexes and propagation lengths of DLSPPWs, calculated by means of the three different methods, are presented in Table II for a constant ridge thickness of $t=600$ nm. The table presents the results of seven different waveguide dimensions, $w=200$ nm to $w=800$ nm. Note that the $t=600$ nm, $w=800$ nm waveguide is not single mode; however, it is included for illustration purposes. The results for constant ridge thickness show some general tendencies. Firstly, the mode effective indexes calculated by means of the EIM-1 and the EIM-2 are larger than those calculated by means of the FEM. The maximum deviation from the FEM results is, however, less than 3%. Secondly, the propagation lengths calculated by means of the EIM-1 and the EIM-2 are longer than those calculated by application of the FEM. The maximum deviation from the FEM results is 10% for the EIM-1 and 33% for the EIM-2. Thirdly, the deviations of the EIM-1 and EIM-2 from the FEM results decrease with increasing ridge width. Lastly, the results show that the EIM-2 is more accurate than the EIM-1 regarding the mode effective index, but results in much larger error in the calculated propagation lengths.

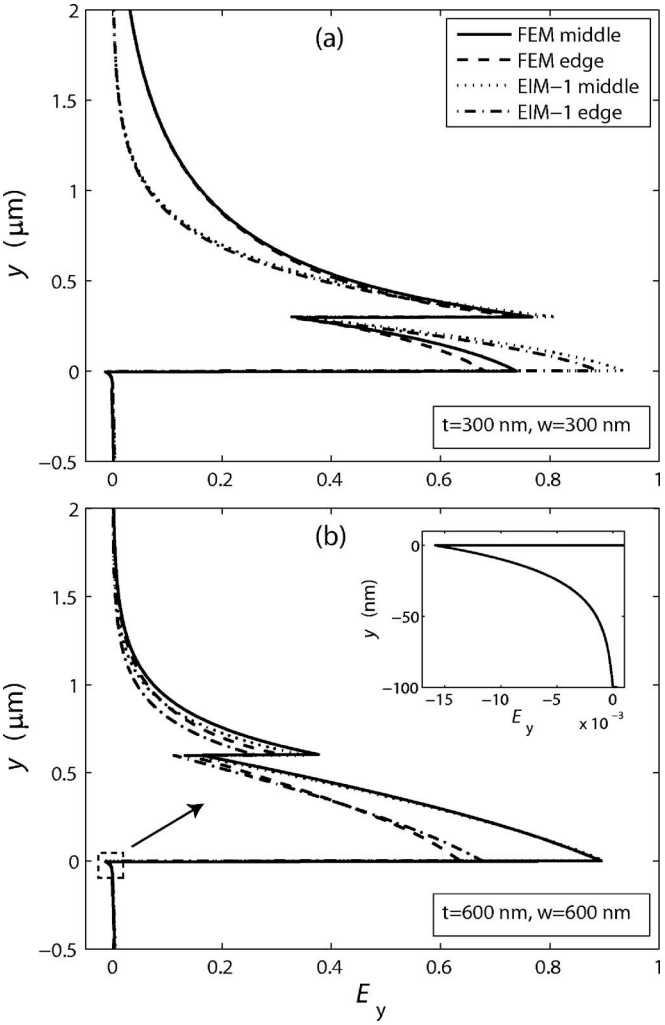

FIG. 12. Vertical profiles of the vertical component of the electric field E_y calculated by utilizing the EIM-1 and the FEM. The edge profiles are taken 50 nm from the vertical edge of the ridge. The field profiles are shown for a $t=300$ nm, $w=300$ nm ridge where $N_{eff,\mathrm{FEM}}=1.04$, $L_{\mathrm{FEM}}=68.7$ μm, $N_{eff,\mathrm{EIM\text{-}1}}=1.08$, $L_{\mathrm{EIM\text{-}1}}=59.7$ μm and for a $t=600$ nm, $w=600$ nm ridge where $N_{eff,\mathrm{FEM}}=1.29$, $L_{\mathrm{FEM}}=44.4$ μm, $N_{eff,\mathrm{EIM\text{-}1}}=1.31$, $L_{\mathrm{EIM\text{-}1}}=45.2$ μm. The inset is a zoom of the EIM-1 middle profile in the metal film.

In Table III, the mode effective indexes and propagation lengths calculated by means of the three methods are presented for ridges with constant width $w=500$ nm and varying thickness from $t=200$ nm to $t=800$ nm. As before, some of

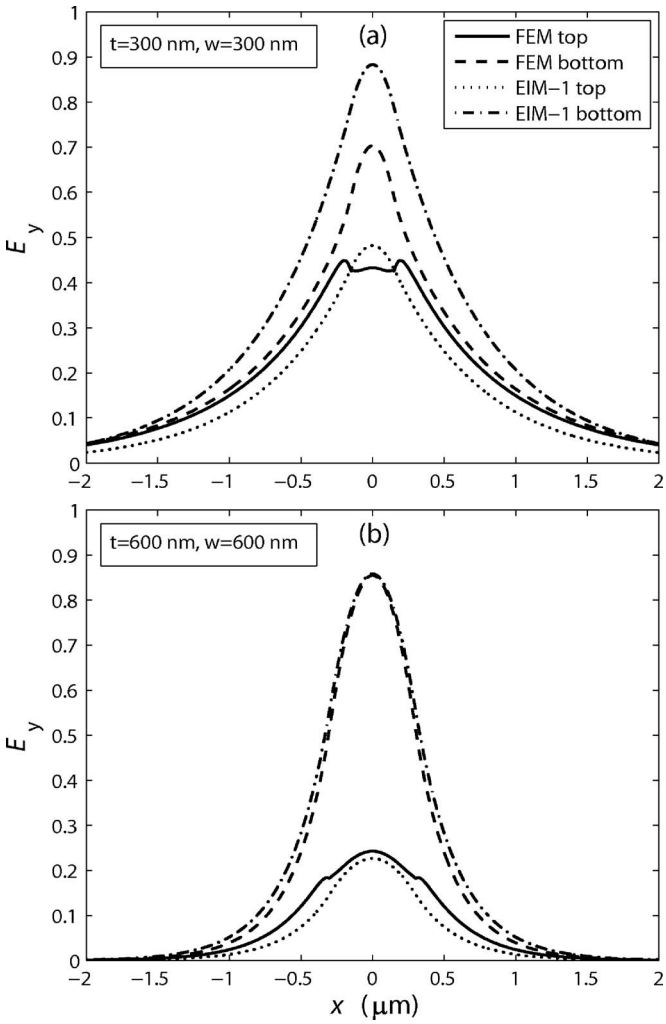

FIG. 13. Lateral profiles of the vertical component of the electric field calculated by utilizing the EIM-1 and the FEM. The bottom profiles are taken 50 nm from the gold-polymer interface and the top profiles are taken 50 nm from the top of the ridge. The field profiles are shown for a $t=300$ nm, $w=300$ nm and for a $t=600$ nm, $w=600$ nm ridge SPP waveguide.

the waveguides are not single mode; however, they are included for illustration purposes. The results of the constant ridge width calculations also show some general tendencies; however, in this case the EIM-2 results are not unambiguously closer to the FEM results regarding N_{eff} and the EIM-1 results are not unambiguously closer to the FEM results regarding the propagation length, as was the case for the constant-thickness waveguide. It is interesting to note that at small ridge thicknesses ($t \lesssim 350$ nm), the accuracy of the EIM-2 regarding N_{eff} is largely affected. This is found to inherit from the approximation that the polymer layer extends infinitely in the vertical direction [Fig. 10(a)], which is a poor approximation for small ridge thicknesses. For larger thicknesses, however, the EIM-2 shows superior results regarding N_{eff} and the EIM-1 is superior regarding the calculation of propagation loss.

The reason for the overestimation of the propagation constant in the EIM can be explained according to previous analysis on dielectric ridge waveguides, where it is found that overestimation occurs when the normalized frequency is large.[25–27] That the accuracy of the propagation length is superior for the EIM-1 is a consequence of the inclusion of the SPP nature of the modes in both steps, whereas the SPP nature of the mode field outside the polymer region, i.e., at the gold-air interface, is not properly accounted for in the EIM-2. This is supported by the following reasoning. An increase in the width of the ridge ($w=300 \rightarrow w=600$ nm) leads to a decrease of the electric field at the gold-air interface outside the ridge [Figs. 8(a) and 8(b)]. Increasing the thickness of the ridge ($t=300 \rightarrow t=600$ nm) does not, however, largely affect the electric field at the interface outside the ridge [Figs. 8(a) and 8(c)]. This implies that if the above explanation of the longer propagation length calculated by the EIM-2 is correct, an increase in ridge width should decrease the error in propagation length of the EIM-2, whereas an increase in thickness should not affect the error largely. This is confirmed in the results presented in Tables II and III as an increase in width ($w=400 \rightarrow w=800$) nm reduces the error from 32% to 19%, whereas an increase in thickness ($t=400 \rightarrow t=800$) nm only reduces the error from 30% to 27%.

The results show that in general the total deviation is larger for the EIM-2 as the error in propagation length is quite large for this method. The error in N_{eff} and L of the EIM-1 for larger ridge dimensions is, however, less than 3% and thus the validity of the EIM-1 proves to be justified except for contemplation of guided SPP modes in very small ridges.

B. Vertical and lateral field distributions

While the accuracy of the mode effective index and propagation length is important for analyzing mode propagation in straight waveguides, the accuracy of the field distribution is of great practical interest in the realization of optical components such as bends, splitters, and directional couplers, because the bend and coupling losses depend strongly on the field distribution (mode confinement) in the cross section of the waveguide. In the EIM-1, field distributions are obtained by taking the product of the lateral and vertical field distributions as calculated in the first and second steps of the EIM-1, respectively, i.e., $E_{\text{EIM-1}}=\psi(x)\phi(y)$ (Fig. 11). Apparent deviations from the FEM result [$E_{\text{FEM}}=E(x,y)$] [Fig. 8(a)] are evident for the $t=300$ nm, $w=300$ nm ridge, especially the discontinuity of the field at $y=300$ nm that accentuates the errors introduced in the EIM-1 by disregarding the corner regions. It is chosen to compare vertical and lateral field profiles obtained from the EIM-1 and FEM field plots to investigate the accuracy of the calculated field distributions further. The field distributions from the EIM-1 and the FEM are normalized so that the surface integrals of E_y^2 in the cross section are equal.

Vertical field profiles taken through the middle of the ridge and 50 nm from the edge of the ridge are found for a $t=300$ nm, $w=300$ nm ridge and a $t=600$ nm, $w=600$ nm ridge (Fig. 12). Lateral field profiles taken 50 nm from the top and 50 nm from the bottom of the ridge are found for the same ridge dimensions (Fig. 13). The field profiles of the

smaller waveguide show that the discrepancy between the two methods is significant in regard to the field distribution. The results of the EIM-1 illustrate that the field is noticeably larger at the metal surface, implying better vertical confinement, but also introducing larger Ohmic losses. The field profiles of the larger structure show a close correlation between the EIM-1 and FEM distributions, implying nearly identical mode confinement. However, whereas the bottom lateral profiles all are Gaussian in shape, the top lateral profiles of the FEM show irregularities at the ridge edges, which are found to inherit from the strong confinement of the electric field around the 90° corners of the ridge. In addition, the squeezing of the field into the ridge and the nonvertical components of the electric field in the smaller structure [Fig. 9(a)] makes these irregularities more apparent there [Fig. 13(a)]. The inset in Fig. 12(b) further confirms that the modes indeed are DLSPPW modes, as the field is shown to decrease exponentially into the metal film.

V. DISCUSSION AND CONCLUSIONS

The characteristics of DLSPPWs have been considered in detail by making use of different simulation methods, i.e., the EIM and the FEM. The validity of two different EI approaches has been evaluated by comparing the computed mode effective indexes, propagation lengths, and vertical and lateral field profiles to those found by means of the FEM. As expected, the EIM results showed noticeable deviations from the FEM results when treating weakly bound DLSPPW modes, whereas for the modes being far from cutoff the EIM was found reasonably accurate. The EIM, in which the DLSPPW was first considered as a planar multilayered waveguide before correcting for the finite width of the ridge (EIM-1), has been proved the most accurate in the whole range, as the other approach (EIM-2) failed to properly account for the field magnitude at the gold-air interface outside the ridge. By analyzing electric-field distributions in the DLSPPW cross sections calculated with the FEM, it has been found that the EIM inaccuracy when treating weakly bound modes inherits from not accounting for the field magnitude in the corner regions. Furthermore, the FEM field vector plots for different DLSPPWs showed that the assumption of linear (vertical) polarization in the EIM introduces an error, which is quite large for close to cutoff waveguides.

The DLSPPW mode effective index, confinement, and propagation length were calculated at the telecom wavelength $\lambda=1.55$ μm for different widths and thicknesses of a polymer ridge placed on a gold film surface. The condition for single-mode guiding has been investigated (using the EIM), and it has been found that single-mode DLSPPW guiding can be realized for ridge thicknesses smaller than ~630 nm and widths below ~655 nm (when decreasing the ridge thickness, the ridge width suitable for single-mode guiding increases). It has also been established that, in contrast to the usual trade-off, the DLSPPW mode lateral confinement can be improved simultaneously with the increase in the mode propagation length by choosing the appropriate ridge thickness [cf. Figs. 4(b) and 6]. In general, for each ridge thickness, the ridge width can be optimized with respect to the mode lateral confinement (Fig. 6). This optimum ridge width ranges from 850 to 500 nm for the thicknesses considered ($t=200$ nm to $t=600$ nm), where a larger ridge thickness implies a smaller mode width. It has thus been found favorable to have as thick a dielectric ridge waveguide as possible allowed by the single-mode condition, both regarding the mode confinement and propagation loss. For telecom wavelengths ($\lambda=1.55$ μm), the EIM calculations showed that a ridge having the thickness of 600 nm and the width of 500 nm would support a DLSPPW mode with the mode width $W=915$ nm, implying the subwavelength confinement (inside the ridge), and the propagation length $L=48$ μm, which is still relatively long. We believe that the presented results improve our understanding of the main features of SPP guiding in DLSPPW structures as well as provide useful guidelines for the design of DLSPPW-based photonic components. We conduct further investigations in this area.

ACKNOWLEDGMENTS

The authors thank Thomas Søndergaard for his help in developing a multilayer waveguide program used in this work and acknowledge the support of the PLASMOCOM project (EC FP6 IST 034754 STREP).

*Electronic address: holmgaard@physics.aau.dk

[1] H. Raether, *Surface Plasmons on Smooth and Rough Surfaces and on Gratings*, 1st ed. (Springer-Verlag, Berlin, 1988).
[2] W. L. Barnes, A. Dereux, and T. W. Ebbesen, Nature (London) **424**, 824 (2003).
[3] J. Takahara, S. Yamagishi, H. Taki, A. Morimoto, and T. Kobayashi, Opt. Lett. **22**, 475 (1997).
[4] M. Quinten, A. Leitner, J. R. Krenn, and F. R. Aussenegg, Opt. Lett. **23**, 1331 (1998).
[5] S. A. Maier, P. G. Kik, H. A. Atwater, S. Meltzer, E. Harel, B. E. Koel, and A. A. G. Requicha, Nat. Mater. **2**, 229 (2003).
[6] R. Zia, M. D. Selker, and M. L. Brongersma, Phys. Rev. B **71**, 165431 (2005).
[7] S. I. Bozhevolnyi, J. Erland, K. Leosson, P. M. W. Skovgaard, and J. M. Hvam, Phys. Rev. Lett. **86**, 3008 (2001).
[8] K. Tanaka and M. Tanaka, Appl. Phys. Lett. **82**, 1158 (2003).
[9] B. Wang and G. P. Wang, Appl. Phys. Lett. **85**, 3599 (2004).
[10] I. V. Novikov and A. A. Maradudin, Phys. Rev. B **66**, 035403 (2002).
[11] D. K. Gramotnev and D. F. P. Pile, Appl. Phys. Lett. **85**, 6323 (2004).
[12] S. I. Bozhevolnyi, V. S. Volkov, E. Devaux, and T. W. Ebbesen, Phys. Rev. Lett. **95**, 046802 (2005).
[13] S. I. Bozhevolnyi, V. S. Volkov, E. Devaux, J.-Y. Laluet, and T. W. Ebbesen, Nature (London) **440**, 508 (2006).
[14] C. Manolatou, S. G. Johnson, S. Fan, P. R. Villeneuve, H. A.

Haus, and J. D. Joannopoulos, J. Lightwave Technol. **17**, 1682 (1999).
[15] B. Steinberger, A. Hohenau, D. Ditlbacher, A. L. Stepanov, A. Drezet, F. R. Aussenegg, A. Leitner, and J. R. Krenn, Appl. Phys. Lett. **88**, 094104 (2006).
[16] C. Reinhardt, S. Passinger, B. N. Chichkov, C. Marquart, I. P. Radko, and S. I. Bozhevolnyi, Opt. Lett. **31**, 1307 (2006).
[17] A. Hohenau, J. R. Krenn, A. L. Stepanov, A. Drezet, H. Ditlbacher, B. Steinberger, A. Leitner, and F. R. Aussenegg, Opt. Lett. **30**, 893 (2005).
[18] A. B. Buckman, *Guided-Wave Photonics*, 1st ed. (Saunders College Publishing, New York, 1992).
[19] H. Kogelnik, *Integrated Optics* (Springer-Verlag, Berlin, 1979).
[20] A. Boltasseva, T. Nikolajsen, K. Leosson, K. Kjaer, M. S. Larsen, and S. I. Bozhevolnyi, J. Lightwave Technol. **23**, 413 (2005).
[21] S. I. Bozhevolnyi, Opt. Express **14**, 9467 (2006).
[22] S. J. Al-Bader, IEEE J. Quantum Electron. **40**, 325 (2004).
[23] P. Berini, Phys. Rev. B **61**, 10484 (2000).
[24] M. P. Nezhad, K. Tetz, and Y. Fainman, Opt. Express **12**, 4072 (2004).
[25] G. B. Hocker and W. K. Burns, Appl. Opt. **16**, 113 (1977).
[26] A. Kumar, D. F. Clark, and B. Culshaw, Opt. Lett. **13**, 1129 (1988).
[27] K. S. Chiang, Opt. Lett. **16**, 714 (1991).
[28] E. D. Palik, *Handbook of Optical Constants of Solids*, 1st ed. (Academic, New York, 1985).
[29] H. Kogelnik and V. Ramaswamy, Appl. Opt. **13**, 1857 (1974).
[30] J. Jin, *The Finite Element Method in Electromagnetics*, 2nd ed. (Wiley, New York, 2002).
[31] T. Itoh, *Numerical Techniques for Microwave and Millimeter-Wave Passive Structures*, 1st ed. (Wiley, New York, 1989).
[32] R. D. Cook, D. S. Malkus, M. E. Plesha, and R. J. Witt, *Concepts and Applications of Finite Element Analysis*, 4th ed. (Wiley, New York, 2002).

CST视频培训课程推荐

CST 微波工作室(CST Microwave Studio)是 CST 工作室套装中最核心的一个子软件，主要用于三维电磁问题的仿真分析，可计算任意结构任意材料电大宽带的电磁问题。广泛应用于高频/微波无源器件的仿真设计、各种类型的天线设计、雷达散射截面分析、电磁兼容分析和信号完整性分析等各个方面。

易迪拓培训(www.edatop.com)推出的 CST 微波工作室视频培训课程由经验丰富的专家授课，旨在帮助用户能够快速地学习掌握 CST 微波工作室的各项功能、使用操作和工程应用。购买 CST 教学视频培训课程套装，还可超值赠送 3 个月免费在线学习答疑，让您学习无忧。

CST 学习培训课程套装

该培训套装由易迪拓培训联合微波 EDA 网共同推出，是最全面、系统、专业的 CST 微波工作室培训课程套装，所有课程都由经验丰富的专家授课，视频教学，可以帮助您从零开始，全面系统地学习 CST 微波工作的各项功能及其在微波射频、天线设计等领域的设计应用。且购买该套装，还可超值赠送 3 个月免费学习答疑…

课程网址：http://www.edatop.com/peixun/cst/24.html

HFSS 天线设计培训课程套装

套装共含 5 门视频培训课程，课程从基础讲起，内容由浅入深，理论介绍和实际操作讲解相结合，全面系统的讲解了 CST 微波工作室天线设计的全过程。是国内最全面、最专业的 CST 天线设计课程，可以帮助您快速学习掌握如何使用 CST 设计天线，让天线设计不再难…

课程网址：http://www.edatop.com/peixun/cst/127.html

更多 CST 视频培训课程：

- **CST 微波工作室入门与应用详解 — 中文视频教程**
  CST 微波工作室初学者的最佳培训课程，由工程经验丰富的资深专家授课，全程中文讲解，高清视频，直观易学。网址：http://www.edatop.com/peixun/cst/25.html
- **CST 微波工作室天线设计详解 — 中文视频培训教程**
  重点讲解天线设计相关知识和使用 CST 进行天线仿真设计的使用操作，是学习掌握使用 CST 微波工作室进行天线设计的必备课程，网址：http://www.edatop.com/peixun/cst/26.html
- **CST 阵列天线仿真设计实例详解 —— 中文视频教程**
  阵列天线设计专业性要求很高，因此相关培训课程是少之又少，该门培训课程由易迪拓培训重金聘请专家讲解；课程网址：http://www.edatop.com/peixun/cst/123.html
- **更多 CST 培训课程**，敬请浏览：http://www.edatop.com/peixun/cst

关于易迪拓培训：

易迪拓培训(www.edatop.com)由数名来自于研发第一线的资深工程师发起成立，一直致力和专注于微波、射频、天线设计研发人才的培养；后于 2006 年整合合并微波 EDA 网(www.mweda.com)，现已发展成为国内最大的微波射频和天线设计人才培养基地，成功推出多套微波射频以及天线设计相关培训课程和 ADS、HFSS 等专业软件使用培训课程，广受客户好评；并先后与人民邮电出版社、电子工业出版社合作出版了多本专业图书，帮助数万名工程师提升了专业技术能力。客户遍布中兴通讯、研通高频、埃威航电、国人通信等多家国内知名公司，以及台湾工业技术研究院、永业科技、全一电子等多家台湾地区企业。

我们的课程优势：

※ 成立于 2004 年，10 多年丰富的行业经验

※ 一直专注于微波射频和天线设计工程师的培养，更了解该行业对人才的要求

※ 视频课程、既能达到现场培训的效果，又能免除您舟车劳顿的辛苦，学习工作两不误

※ 经验丰富的一线资深工程师讲授，结合实际工程案例，直观、实用、易学

联系我们：

※ 易迪拓培训官网：http://www.edatop.com

※ 微波 EDA 网：http://www.mweda.com

※ 官方淘宝店：http://shop36920890.taobao.com